



HAL
open science

Reduction of a two-dimensional crystalline MoO₃ monolayer

Svetlozar Surnev, Jacek Goniakowski, Malihe Mohammadi, Claudine Noguera,
Falko Netzer

► **To cite this version:**

Svetlozar Surnev, Jacek Goniakowski, Malihe Mohammadi, Claudine Noguera, Falko Netzer. Reduction of a two-dimensional crystalline MoO₃ monolayer. *Surface Science: A Journal Devoted to the Physics and Chemistry of Interfaces*, 2024, 750, pp.122579. 10.1016/j.susc.2024.122579. hal-04684669

HAL Id: hal-04684669

<https://hal.science/hal-04684669>

Submitted on 3 Sep 2024

HAL is a multi-disciplinary open access archive for the deposit and dissemination of scientific research documents, whether they are published or not. The documents may come from teaching and research institutions in France or abroad, or from public or private research centers.

L'archive ouverte pluridisciplinaire **HAL**, est destinée au dépôt et à la diffusion de documents scientifiques de niveau recherche, publiés ou non, émanant des établissements d'enseignement et de recherche français ou étrangers, des laboratoires publics ou privés.

Reduction of a two-dimensional crystalline MoO₃ monolayer

Svetlozar Surnev^{1*}, Jacek Goniakowski^{2*}, Malihe Mohammadi¹, Claudine Noguera², and Falko P. Netzer¹

¹*Surface and Interface Physics, Institute of Physics, Karl-Franzens University, 8010 Graz, Austria*

²*CNRS - Sorbonne Université, Institut des Nanosciences de Paris, UMR 7588, 75005 Paris, France*

Abstract

The atomic structure of MoO_x films formed upon a gradual thermal reduction of an ordered MoO₃ monolayer on the Pd(100) substrate was explored via surface science characterization techniques and density functional theory (DFT) calculations. Two main reduction stages were identified. First, the initial oxygen excess was gradually eliminated by altering the domain boundary length, orientation, and atomic structure. The films nevertheless remained O-rich, with numerous terminal oxygen atoms (formation of Mo=O groups), and an elevated work function. Second, multiple ordered O-lean phases were formed, characterized by either very few or no terminal oxygen atoms, and a much smaller surface work function. According to calculations, the positive charging of the Pd substrate stabilizes the oxygen excess during the first stage, but during the second reduction stage, the substrate becomes negatively charged, stabilizing enhanced cation oxidation states. On their basis, the mechanisms underlying the oxygen release from the initial c(2x2) domains were disclosed. The experiments showed that the film reduction is perfectly reversible, which highlights the very promising properties of the MoO₃/Pd system for heterogeneous catalysis.

Keywords

Molybdenum oxides, Palladium, 2D oxides, redox reactions, STM, DFT

* Corresponding authors

E-mails: svetlozar.surnev@uni-graz.at; jacek.goniakowski@insp.jussieu.fr

1. Introduction

Reducible oxides constitute excellent catalyst materials with particular activity in oxidation reactions following the Mars-van Krevelen mechanism [1], that is with the participation of lattice oxygen as oxidizing agent. Oxide reducibility is associated with oxygen vacancy creation and a concomitant decrease of the oxidation state of the cations, with a change in composition from MO_x to $\text{MO}_{x-\delta}$ [2]. MoO_3 is a prototypical reducible oxide with many applications of physics and chemistry in diverse areas of surface technologies, nanosystems and devices [3]: this flexible applicability is intimately connected with the easy change of the oxidation state of the Mo cations. The reducibility of oxides can be enhanced, with respect to the related bulk material, by nanostructuring and by the proximity of the oxide phase to a metallic interface [2]. Here we report a detailed study of the reduction of such a system, namely a two-dimensional (2D) crystalline MoO_3 nanophase supported on a Pd(100) single crystal surface, using atomic precision surface science methodology in conjunction with extended DFT calculations.

MoO_3 in bulk form supports two modifications: the orthorhombic α -phase and the monoclinic β -phase. α - MoO_3 consists of a series of bilayers, stacked perpendicular to the [010] direction; each layer contains two sublayers of distorted MoO_6 octahedra, joined together by edge and corner sharing. The bilayers are held together by van der Waals-type interactions. The MoO_3 α -phase is the thermodynamically stable polymorph. The monoclinic β -phase is similar to the stable room-temperature phase of WO_3 and is derived from a distorted ReO_3 structure; the MoO_3 β -phase is only metastable.

Previous work has investigated the formation of vacancies on surfaces of MoO_3 and the related WO_3 in studies of the structure of the respective single crystal surfaces. A number of surface superstructures and surface reconstructions have been reported during the surface preparation of WO_3 (001) single crystal surfaces. These have been associated with the formation of oxygen vacancies and the corresponding defect structures have been related to the ordering of oxygen vacancies on the partly reduced surfaces [4-10]. The (010) surface of a single crystal MoO_3 sample has been investigated in the early work of Firment and Ferretti [11] by electron spectroscopy and O defect related states have been interpreted in terms of crystallographic shear planes, in analogy to those encountered in the MoO_3 bulk phase [12]. The reduction of thin films of MoO_3 has been followed by XPS [13,14] and the electronic and optical properties of reduced Mo oxide phases have been addressed by DFT [14]. Of more direct relevance to the present work is the thermal reduction study of a well-ordered single-layer MoO_3 nanostructure

supported on Au(111) [15]: upon annealing to 650 K oxygen vacancies and the formation of reduced Mo^{5+} species have been observed. Deng et al. [15] have suggested that the thermal reduction leads to the creation of O vacancies in the form of 2D shear defects, in contrast to the 3D shear structures observed in reduced bulk MoO_3 .

This present work is based on our previous study of the evolution of 2D MoO_3 nanolayer structures on Pd(100) [16,17], where a robust MoO_3 monolayer nanocrystal has been grown and fully characterized at the atomic level. This well-ordered oxide monolayer with a $c(2 \times 2)$ surface structure (with respect to the Pd(100) substrate) allows us to study the thermal reduction of a 2D MoO_3 nanostructure with atomic precision. The reduction process has been followed step-by-step using atomic resolution scanning tunneling microscopy (STM), LEED, X-ray photoelectron spectroscopy (XPS) and DFT calculations to reveal a comprehensive picture of the reduction process. A sequence of several ordered 2D surface phases has been observed during the reduction. They range from O-rich, characterized by an oxygen excess and numerous $\text{Mo}=\text{O}$ groups linking Mo atoms to one terminal oxygen atom, to O-lean, with ring-wise structures and only few terminal oxygen atoms. DFT calculations elucidated the electronic structure characteristics, the different stabilizing role of the Pd substrate in these two reduction stages, and the associated variations of the surface work function. Finally, on their basis, the mechanisms underlying the oxygen release from the initial $c(2 \times 2)$ domains were disclosed.

2. Methods

2.1. Experimental Section

The experiments were performed in two custom-designed ultrahigh vacuum (UHV) chambers, one for scanning tunneling microscopy (STM) and the second for x-ray and ultraviolet photoelectron spectroscopy (XPS and UPS) measurements, both with typical base pressures $p < 1 \times 10^{-10}$ mbar and equipped with the usual facilities for crystal cleaning, LEED optics, and physical vapor deposition. The STM system contains a variable-temperature STM (Oxford Instruments), where STM images were collected in a constant current mode at room temperature or at elevated temperatures. Electrochemically etched tungsten tips were used, which were cleaned *in situ* by electron bombardment. If not explicitly stated in the text, bias voltages (referenced with respect to the sample) were varied between +0.1 V and +2.0 V, and tunneling currents were set between 10 pA and 100 pA. The XPS/ UPS system is supplied with a dual x-ray source for Mg $K\alpha$ and Al $K\alpha$ radiation, a He discharge lamp for He I and He II

radiation and a hemispherical electron analyzer (PHOIBOS 100, SPECS). Mg $K\alpha$ radiation was used to excite the Mo 3d XPS core levels and the O KLL Auger lines, with a spectral resolution of ~ 0.7 eV. The background-subtracted Mo 3d spectra were decomposed into individual core-level components using least-square fits with convoluted Gauss-Lorentzian lineshapes. The secondary electron cut-offs in the He I UPS spectra were used to estimate the absolute work function of the investigated surfaces.

In all UHV systems the Pd(100) surfaces were cleaned by several cycles of Ar-ion sputtering and annealing to 1000 K. The $c(2 \times 2)$ -MoO₃ monolayer surface was prepared by the deposition of (MoO₃)₃ clusters in UHV onto the clean Pd(100) surface. The (MoO₃)₃ cluster beam was generated by thermal sublimation of a MoO₃ powder at ~ 780 K in an effusion cell evaporator, with the evaporation rate monitored by a quartz-crystal microbalance (QMB). One monolayer (1 ML) is defined by the density of the $c(2 \times 2)$ -MoO₃ surface plane with a lattice constant of 3.89 Å (6.61×10^{14} MoO₃ units·cm⁻²) [16]. Taking the molecular mass of MoO₃ into account, 1 ML MoO₃ on Pd(100) correspond to a frequency change in the QMB of 15.8 Hz.

2.2. DFT Calculations

DFT calculations were carried out using the Vienna Ab-initio Simulation Package (VASP) [18,19], the Projector Augmented Wave approximation [20,21] to simulate the electron-core interaction, and a 400 eV energy cutoff in the expansion of Kohn-Sham orbitals on a plane-wave basis set. As in the previous studies [16,17], the present spin-unrestricted calculation used the PBEsol [22] exchange-correlation functional with the DFT+U method suggested by Dudarev [23,24], and the U_{Mo} value was fixed at 4.0 eV. Ionic charges were approximated using Bader's partition technique [25,26], and magnetic moments were calculated by integrating the spin density within the Bader volumes. It is essential to highlight that the distinct local environments of cations in the supported nanostructures require the simultaneous use of both Bader charges q_{Mo} and magnetic moments μ_{Mo} for a reliable determination of formal Mo oxidation states. Indeed, while the Mo ions in bulk MoO_x crystals provide a first reference ($q_{\text{Mo}} = +2.7, +2.5, \text{ and } +2.2$ e and $\mu_{\text{Mo}} = 0.0, 0.8, \text{ and } 1.9 \mu_{\text{B}}$ for Mo in 6+, 5+, and 4+ oxidation states, respectively, as deduced from results for MoO₃, Mo₈O₂₃, and MoO₂ bulk phases, respectively), the complexity of the supported nanostructures necessitates a more comprehensive analysis. The Tersoff-Hamann approximation was used for STM image simulations [27], and atomic configurations were plotted using VESTA [28].

We analyzed various MoO_x films in ($\sqrt{2} \times \sqrt{2}$)-, (6 x 7)-, ($\sqrt{5} \times \sqrt{5}$)-, (4 x 4)-, and (3 x 3)-Pd(100) unit cells with the experimental in-plane bulk Pd lattice parameter (3.89 Å). The Brillouin zone of the ($\sqrt{2} \times \sqrt{2}$) cell was sampled using a Γ -centered (6 x 6) Monkhorst-Pack mesh and the same sampling density was used for the other cells. Following the earlier studies [16,17], the Pd substrate was approximated by a slab made up of three (100) atomic planes, with the oxide film placed on one side of the slab. Slabs were separated by more than 10 Å of vacuum and dipole corrections were applied. The atomic coordinates of all anions, cations, and Pd atoms were relaxed until forces dropped below 0.01 eV Å⁻¹, except for the bottom-most Pd layer, which remained in its bulk-like position.

Atomic structures of Pd-supported Mo_nO_m films were initially optimized using a homemade genetic algorithm (GA) similar to those used in recent studies on metal-supported Al₂O₃ [29,30] and CrO_x [31] films, or NbO_x [32] clusters. For each Mo_nO_m composition in a given unit cell, a large number of random configurations were first generated and relaxed. The subsequent GA iterations consisted of (i) randomly selecting 'parent' structure(s) with a bias towards more stable ones, (ii) applying genetic operators (principally cut-and-splice crossover and rattle mutations) to the parent structure(s) to create a set of 'child' configurations, and (iii) relaxing these 'child' structures, with the most stable ones becoming the 'parent' generation in the next step. At each iteration, the overall convergence was monitored with the 20 most stable DFT-optimized configurations. The global optimization was based on an efficient machine-learned force field developed, improved, and applied with VASP. The initial training set consisted of DFT forces and energies for several tens of randomized MoO_x/Pd(100) structures, and was further complemented with DFT results obtained during the subsequent GA iterations.

3. Experimental results

3.1. LEED and STM characterization

Before starting to investigate the structural changes occurring during the thermal reduction of the c(2x2)-MoO₃ monolayer on Pd(100), it is necessary to introduce shortly its main structural characteristics, established previously [16,17]. Figure 1 shows a collection of LEED (a) and STM images (b-d) taken in this study, which are exemplary for the MoO₃ monolayer. Large-scale STM images (Fig. 1b) reveal a highly-ordered pattern of square domains with a mean size of 3.5 ± 0.5 nm, which are separated by straight and narrow domain boundaries oriented parallel

to the [001] and [010] Pd directions. Within the domains a $(\sqrt{2}\times\sqrt{2})\text{-R}45^\circ$ (or equivalently $c(2\times 2)$) surface structure with a lattice parameter of 3.9 Å is atomically resolved (Figs. 1b,c). Neighboring domains are lined up antiphase to each other, causing a characteristic splitting of the $(1/2, 1/2)$ fractional order spots in the LEED pattern (Fig. 1a). The DFT-derived structure model (Fig. 1e) of the $c(2\times 2)$ - MoO_3 monolayer on Pd(100) consists of a planar $c(2\times 2)$ MoO_2 layer, where each Mo atom is terminated on top by an additional O atom [16,17], imaged bright in STM. Defects in the form of missing terminal oxygen atoms generate dark depressions in the STM images (Figs. 1c,d), whose surface density in the as-prepared $c(2\times 2)$ - MoO_3 monolayer is estimated to be below 1%. An important consequence of the particular domain structure of the MoO_3 monolayer on Pd(100) is that about 40% of the Mo atoms are located along the [01] and [10] edges at the domain boundaries, and exhibit a more O-rich character than those inside the domains (the formal film stoichiometry is thus close to $\text{MoO}_{3.2}$), due to the charge transfer from the Pd substrate needed to compensate the edge polarity [17]. This will translate into an enhanced reducibility at the domain boundaries, as it will be shown in the following.

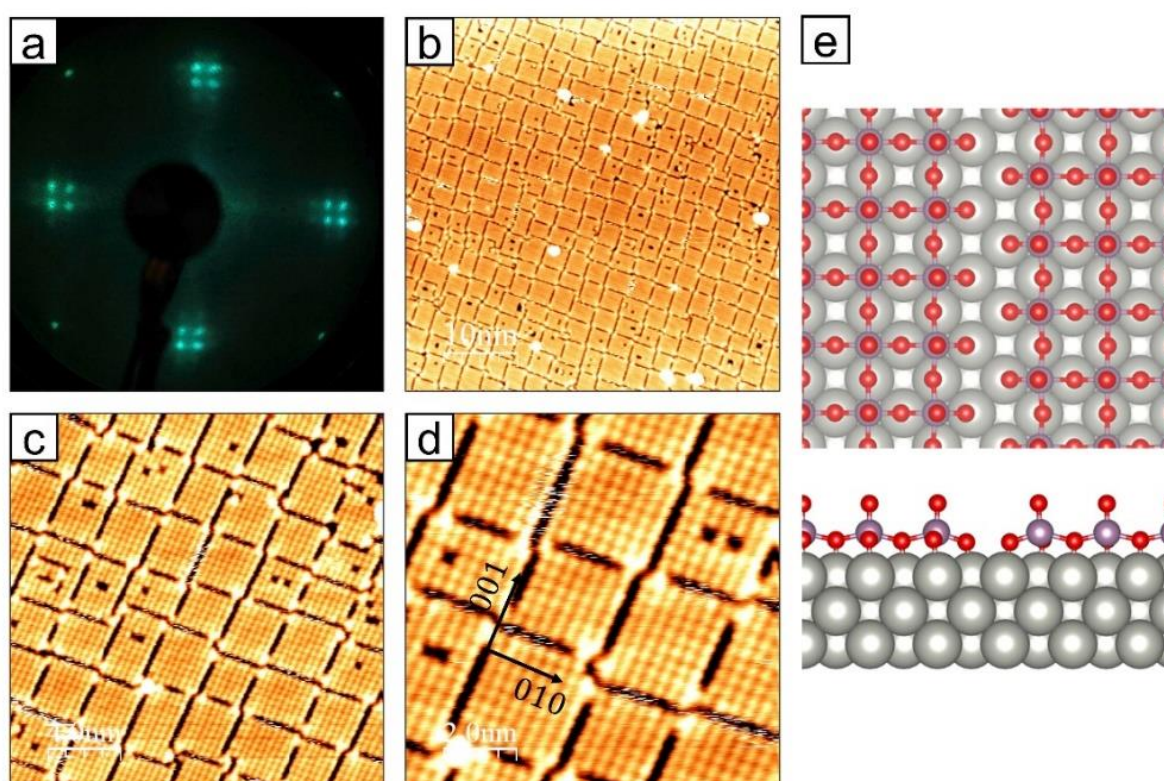


Fig. 1. LEED (a) and STM images (b-d) of the $c(2\times 2)$ - MoO_3 monolayer on Pd(100); (e) Top (upper panel) and side view (bottom panel) of the DFT structure model (adapted from Ref. [17]). Oxygen, molybdenum and palladium atoms are shown as red, blue, and gray coloured circles, respectively.

Figure 2 illustrates the structural changes, as monitored by LEED and STM, after 5 min UHV annealing the MoO_3 monolayer on Pd(100) to 623 K (a-d) and 673 K (e-h). The first annealing

step at 623 K causes significant modifications of the size and shape of the MoO₃ domains: notably, the average domain size increases by about a factor of two, from 3.5 nm to 6.5 nm, and the shape of the domains becomes more irregular, exposing also [11] edges (Fig. 2b,c). The domain boundaries are not straight anymore, but exhibit zig-zag character due to the presence of bright triangular features (Fig. 2c,d) signaling reduction at the boundaries. A similar triangular-shaped reconstruction has been previously reported for a Na-doped MoO₃ monolayer on Pd(100), and attributed to a Na-induced O loss at the domain boundaries [16]. The O vacancies, initially present within the domains, are healed out by the annealing, probably migrating towards the domain edges. In the LEED pattern (Fig. 2a) the splitting of the fractional order spots of the pristine surface is replaced by streaks, which can be associated with the large scatter in the domain size observed in STM (Fig. 2b).

After the next annealing step at 673 K the LEED pattern (Fig. 2e), although becoming more diffuse, does not change significantly, and the c(2x2) structure remains the dominant oxide phase, as also corroborated by the STM images (Fig. 2f-h). However, large-scale STM images (Fig. 2f) reveal that the c(2x2) monolayer (labeled A) locally breaks apart, being partially replaced by deeper lying areas (labeled B and C) appearing with darker contrast in STM. The line profile across such areas (inset in Fig. 2f) display two different height levels with apparent depths of approximately 1 Å (areas B) and 1.5 Å (small patches C) below the c(2x2) surface. The latter value is compatible with the apparent height of the c(2x2) monolayer with respect to the bare Pd(100) surface [17]. The B areas do not exhibit any structural order at this annealing stage. In the c(2x2) monolayer, a new type of antiphase domain boundaries develops, which appear as zig-zag lines running parallel to the Pd<110> directions in the STM images (Fig. 2g). A more detailed view (Fig. 2h) reveals that these zig-zag lines form a lattice with a rectangular unit cell and size of 1.9 nm x 1.6 nm, corresponding to a (7x6) superlattice. A DFT structure model of this c(2x2)-related phase will be presented below in Section 4. In other c(2x2) areas small square depressions are observed in the STM images (see e.g. Fig. 2f), which are attributed to several missing terminal O atoms in the c(2x2)-MoO₃ monolayer structure. We suppose that the oxide layer left behind after the removal of these oxygen species corresponds to the B areas in the STM images (Figs. 2f,g).

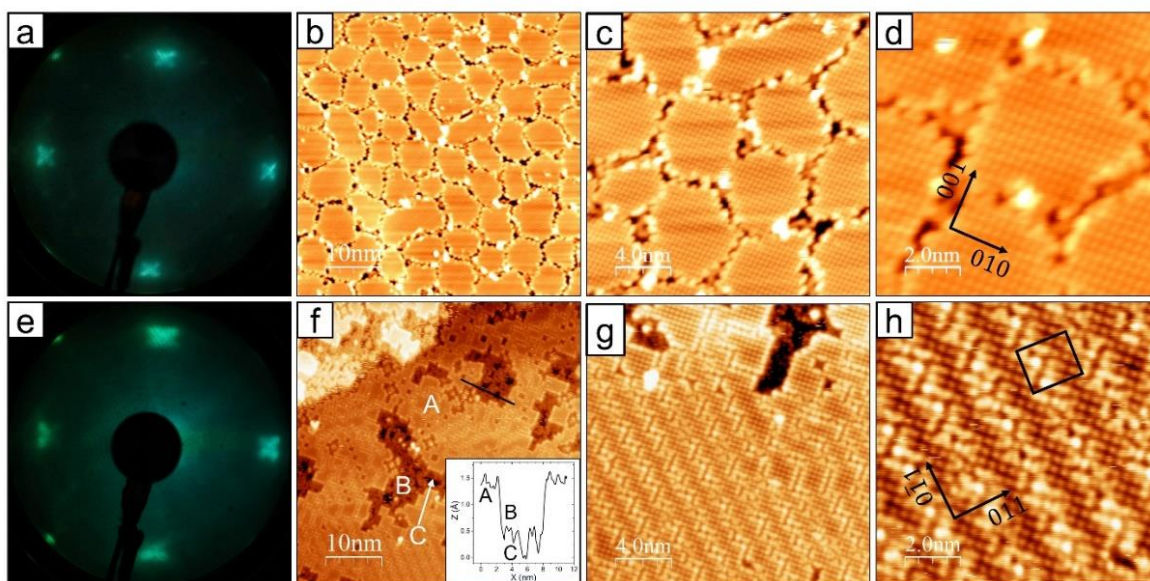


Fig. 2. LEED and STM images of the $c(2 \times 2)$ - MoO_3 monolayer on Pd(100) annealed for 5 min in UHV to 623 K (a-d) and 673 K (e-h), respectively. The areas labelled A in Fig. 2f denote the $c(2 \times 2)$ - MoO_3 layer, whereas those indicated B and C are by $\sim 1.0 \text{ \AA}$ and 1.5 \AA deeper, respectively, as seen from the line profile across the black line shown in the inset. The (7×6) unit cell of the zig-zag structure is drawn as black rectangle in Fig. 2h.

Summarizing the results of this first reduction stage, annealing to 623 K in UHV causes a restructuring of the domain structure in the $c(2 \times 2)$ - MoO_3 monolayer and a significant increase of the domain size. The domain boundaries are not straight anymore, but decorated with triangular-shaped features as a result of oxygen loss. Further annealing to 673 K generates a (7×6) zig-zag lattice out of the pristine $c(2 \times 2)$ layer, and triggers further reduction via the removal of terminal O atoms from the MoO_3 monolayer, initiating a break-up of the oxide film.

The second reduction stage begins with the formation of a new phase displaying a (4×4) LEED pattern (Fig. 3a) following 5 min annealing at 723 K. The large scale STM image in Fig. 3b shows a network of bright dots coexisting with areas of lower STM contrast. Although visually no particularly good long-range order can be recognized in the STM image, the corresponding Fast-Fourier-Transform (FFT) reveals a square pattern (inset in Fig. 3b) corresponding to a real-space periodicity of 1.1 nm, consistent with the (4×4) LEED pattern. The atomically-resolved STM images in Fig. 3c,d show that the $c(2 \times 2)$ - MoO_3 islands decompose into smaller structural units, such as tetramers, dimers, and eventually to monomers, with the latter forming the (4×4) lattice. Each monomer represents a pyramidal MoO_5 unit with four O atoms in the basal plane and one O atop, and this concept agrees well with their cross-like appearance in the STM images (see e.g. Figs. 3g,h).

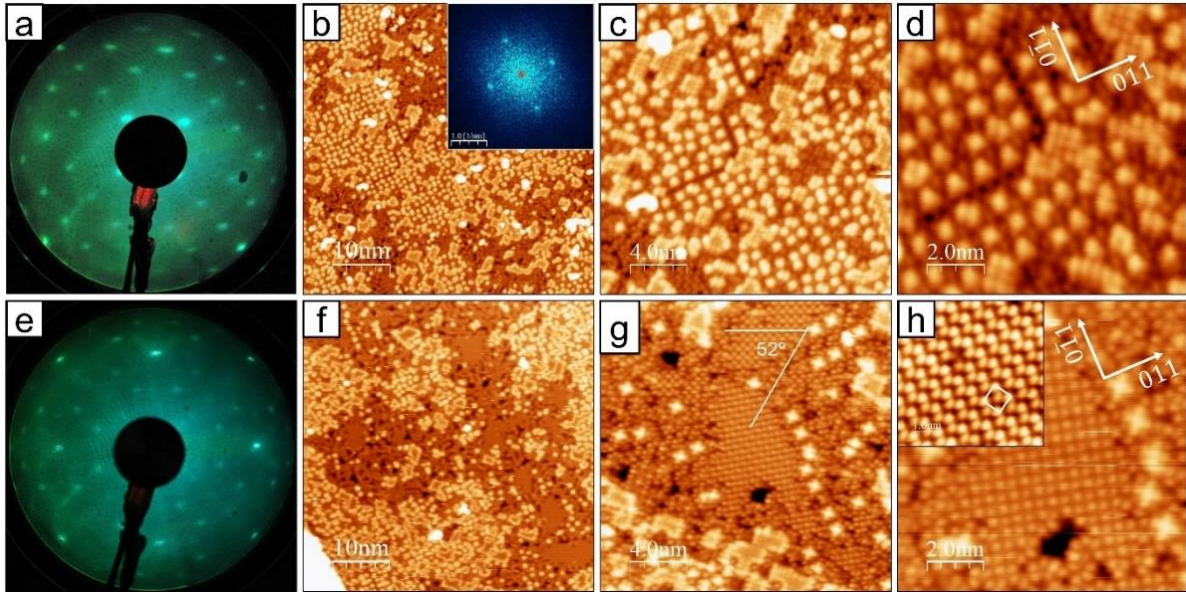


Fig. 3. LEED and STM images of the $c(2 \times 2)$ - MoO_3 monolayer on Pd(100) annealed for 5 min (a-d) and 10 min to 723 K (e-h), respectively. A FFT of the STM image in Fig. 3b is shown in the inset. The inset in Fig. 3h shows a high-resolution STM image of $(\sqrt{5} \times \sqrt{5})R26.6^\circ$ phase taken at a bias of +140 mV; the unit cell is drawn with a white square.

Additional 5 min annealing at 723 K causes the replacement of the (4×4) phase by a new structure, which exhibits in LEED a pattern consisting of diffraction spots arranged in octagons around the half-order spots (Fig. 3e). Large-scale STM images (Fig. 3f) show that the new structure evolves in the areas imaged with a lower contrast, which have now grown at the expense of the (4×4) phase. A more detailed look (Fig. 3g,h) unveils a square lattice with a size of $6.0 \pm 0.1 \text{ \AA}$, indicated with a white square in Fig. 3h, with the unit cell vectors rotated by 26° with respect to the Pd $\langle 110 \rangle$ directions. This gives rise to the occurrence of this structure in two rotational domains, enclosing an angle of 52° with respect to each other, as exemplified by the guiding lines in Fig. 3g. Depending on their orientation with respect to the scanning direction, the domains appear either as zig-zag lines (yellow line in Fig. 3g), or as a square lattice (blue line in Fig. 3g). Given these lattice dimensions and orientations, we identify the new phase as a commensurate $(\sqrt{5} \times \sqrt{5})R26.6^\circ$ structure. Near its edges few isolated (4×4) remnants can be also detected. Note that the $(\sqrt{5} \times \sqrt{5})R26.6^\circ$ structure is a true Mo-oxide related phase and should not be mixed up with the isostructural Pd(100)-O surface oxide, which forms on exposing the bare Pd(100) surface under stronger oxidative conditions than in the present experiment, and displays completely different fingerprints in STM [33,34].

To summarize, the second reduction stage is characterized by the formation of two new ordered oxide phases with (4×4) and $(\sqrt{5} \times \sqrt{5})R26.6^\circ$ structures. Whereas the former one emerges as a

decay product of the $c(2 \times 2)$ MoO_3 monolayer in the form of MoO_5 monomers, the latter has no relation to the pristine surface and corresponds to a kind of reconstructed MoO_2 layer left behind after the removal of the terminal O species. DFT-derived confirmation and structure models of the reduced (4×4) and $(\sqrt{5} \times \sqrt{5})R26.6^\circ$ phases will be presented below in the theoretical part.

The reduction process of the $c(2 \times 2)$ - MoO_3 monolayer is completed after additional 10 min annealing in UHV to 723 K with the formation of a well-ordered (3×3) phase, as demonstrated by the sharp LEED pattern (Fig. 4a) and the presence of large surface areas with low defect density in the STM images (Fig. 4b). The (3×3) phase displays a pronounced bias dependence in STM, illustrated in Figs. 4c-4f, which will be used below for comparison with simulated images from possible structure models. Annealing above 723 K results in the decomposition of the (3×3) phase and thermal desorption of the remaining oxide fragments from the Pd(100) surface.

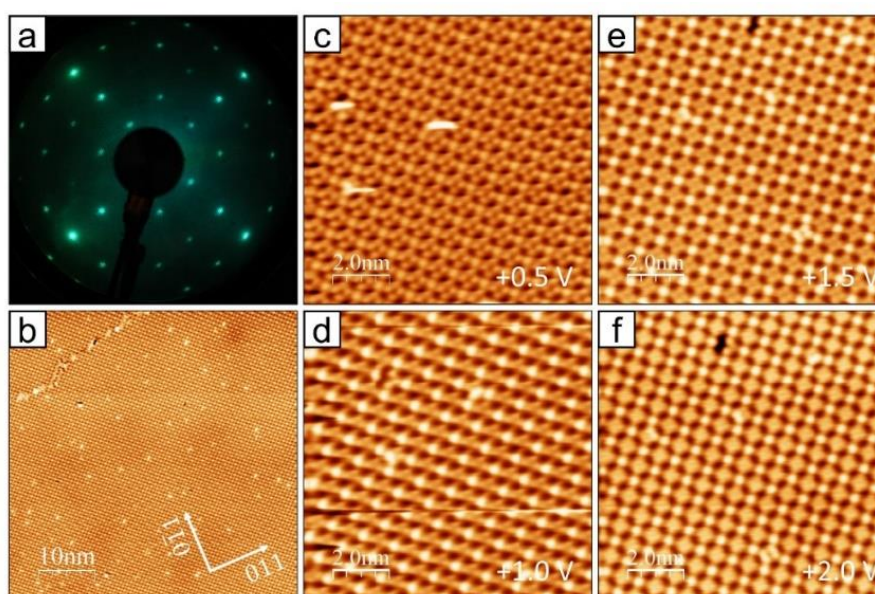


Fig. 4. LEED (a) and STM images (b-f) of the $c(2 \times 2)$ - MoO_3 monolayer on Pd(100) annealed for 20 min to 723 K. The STM images in (c-f) have been taken at bias voltages of +0.5, +1.0, +1.5 and +2.0 V, respectively.

In view of the relevance of molybdenum oxides in the industrial heterogeneous catalysis, where cycling between reducing and oxidizing conditions is commonly performed to activate the catalyst material, it is of interest to test the reversibility of the reduction process of the MoO_3 monolayer in an oxidizing environment. For this purpose, the (3×3) Mo-oxide layer was exposed to an oxygen pressure of 5×10^{-8} mbar at 523 K and the structural changes were monitored *in operando* by STM, that is in the oxygen pressure at elevated temperature. The oxidising pressure and temperature were selected somewhat lower than those used for the $c(2 \times 2)$ - MoO_3 preparation (see Methods, Experimental Section) in order to follow the induced

changes within the time scale of the STM scanning speed. Prior to the oxygen exposure the sample has been tempered for about 45 min in UHV at 523 K in the STM to minimize the thermal drift. The STM image in Fig. 5a shows the (3x3) surface immediately before opening the oxygen valve at the end of the scan; each image takes about 80 s. In the following image (Fig. 5b), small square clusters with edges oriented parallel to the Pd<010> directions nucleate within the (3x3) layer, and their density increases rapidly towards the end of the scan. In the next image (Fig. 5c) the clusters merge together into larger islands, which grow in size with the oxidation time, forming a nearly closed layer on approaching the end of the scan. After 400 s (Fig. 5d) the reoxidation is completed and the surface is covered with irregularly shaped islands, whose edges exhibit a significant frizziness due to the enhanced mass transport at 523 K. Although this inhibits obtaining atomic resolution here, these islands most likely correspond to $c(2 \times 2)$ -MoO₃ domains, akin to those reported in Figs. 2b-d.

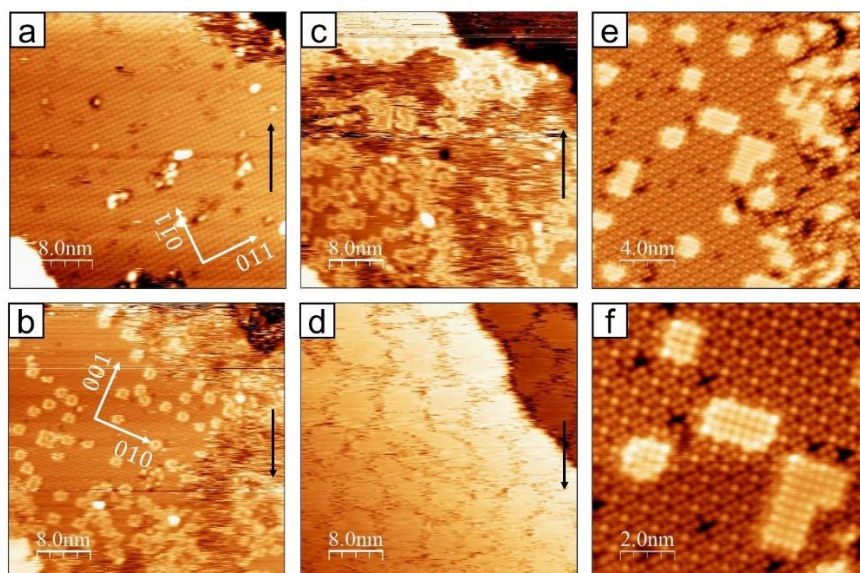


Fig. 5. A sequence of STM images taken during exposing the (3x3) surface (a) in 5×10^{-8} mbar oxygen at 523 K for 80s (b), 160 s (c) and 400 s (d). The arrows indicate the slow scanning direction. The STM images in (e) and (f) have been taken after exposing the (3x3) surface with a similar oxygen dose at 523 K, as that in (b), and subsequently cooled down to room temperature.

This becomes indeed evident from the room-temperature STM images in Figs. 5e,f, which have been taken after an integral oxygen dose of $\sim 1L$, similar to that in Fig. 2b, and cooling to room temperature. Here, small $c(2 \times 2)$ islands of different size are atomically resolved together with the coexisting (3x3) layer. This observation implies that the latter is directly transformed into the MoO₃ monolayer phase without formation of any intermediate phases, like the (4x4) and $(\sqrt{5} \times \sqrt{5})R26.6^\circ$ structures; the latter are probably the result of kinetic effects. The redox transition between the $c(2 \times 2)$ and (3x3) Mo-oxide phases is thus completely reversible and can be repeated many times.

3.2. XPS and work function results

Figure 6 shows a collection of Mo 3d XPS (a) and O KLL (b) Auger spectra taken from the pristine $c(2 \times 2)$ - MoO_3 surface (spectra 1) and after annealing in UHV at increasing temperature and times (spectra 2-10). In between the corresponding LEED patterns are presented. The O KLL Auger spectra were preferred here instead of the O 1s XPS spectra, since the latter partially overlap with the intense Pd 3p substrate peak. The Mo 3d spectra exhibit significant changes, both in line shape and binding energy positions, signaling oxide reduction; these will be analyzed in more detail for selected Mo 3d spectra in Fig. 6e. In contrast, the peak positions of the corresponding O KLL spectra are less sensitive to the Mo oxidation state, but their intensity has dropped by about a factor of 2 between spectrum 1 and 10, a clear proof for the reduction of the oxide layer. To extract a quantitative information on the progress of reduction we have plotted in Fig. 6c the ratio of the integral intensities of the O KLL and Mo 3d peaks (left Y-axis) for the different spectra in Figs. 6a,b as a function of a reduction coordinate involving both the annealing temperature and time. This ratio can be directly converted into the O/Mo atomic ratio in the oxide film (right Y-axis) using the known stoichiometry of the full $c(2 \times 2)$ - MoO_3 monolayer. As the temperature is increased, the O/Mo ratio drops initially and reaches a plateau in the region where the (4×4) structure is observed in the LEED. Longer annealing at 723 K leads to a further decrease in the O/Mo ratio, which can be related with the replacement of the (4×4) by the $(\sqrt{5} \times \sqrt{5})R26.6^\circ$ structure. This trend continues at 753 K, reaching an O/Mo ratio of about 1.5 as the (3×3) structure is well developed in the LEED. Note that the annealing temperatures in the XPS experiments are slightly higher than in the STM, which we ascribe to small temperature reading variations in the different UHV systems.

Similar changes are also observed in the work function, as measured from the secondary electron cut-off in the UPS spectra (not shown) and displayed in Fig. 6d. The work function of the pristine $c(2 \times 2)$ - MoO_3 surface has a value of 6.5 eV, which is by 1.2 eV higher than of the clean Pd(100) surface, which is due to the electrostatic dipole created by the large electron transfer from the Pd substrate [17]. The strong initial decrease of the work function in the transition between the $c(2 \times 2)$ and (4×4) structures can be attributed to the reduced dipole moment associated with the removal of terminal O species from the MoO_3 monolayer, as discussed in more detail in Sect. 4.2. The work function reaches the value of ~ 5.6 eV in the (3×3) phase, which is by 0.9 eV lower than of the pristine $c(2 \times 2)$ surface.

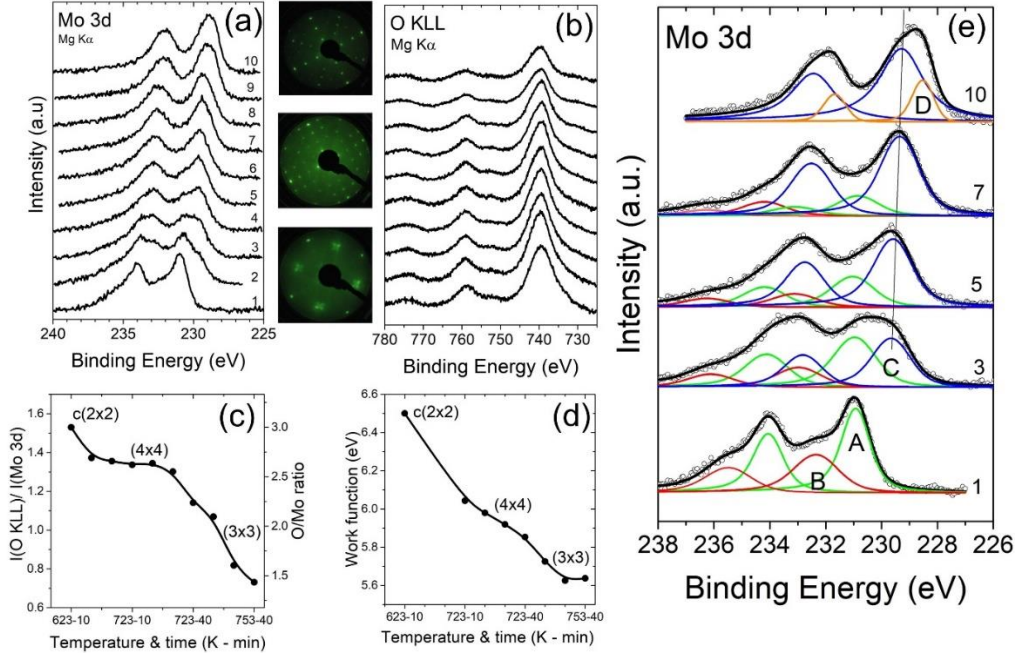


Fig. 6. Mo 3d (a) O KLL (b) spectra of $c(2 \times 2)$ - MoO_3 monolayer (bottom spectra 1) and after annealing in UHV to the following temperature/times: 2 – 673 K /10 min, 3 – 723 K /5 min, 4 – 723 K /10 min, 5 – 723 K /15 min, 6 – 723 K /30 min, 7 – 723 K /45 min, 8 – 723 K /60 min, 9 – 753 K /20 min, and 10 – 753 K /40 min. The corresponding LEED patterns are shown in the inset; (c) Plot of the ratio of the integral intensities of the O KLL and Mo 3d peaks (left Y-axis) versus the annealing temperature and time. The right Y-axis corresponds to the calculated O/Mo ratio in the film. The LEED structures are indicated in the regions of their occurrence; (d) Plot of the work function versus the annealing temperature and time; (e) Least-square fits of selected Mo 3d spectra using different core-level components, indicated A-D, as discussed in the text.

Finally, we discuss the results of the peak deconvolution analysis of selected Mo 3d spectra presented in Fig. 6e. These spectra have been least-square fitted with different core-level components consisting of spin-orbit Mo $3d_{5/2}$ - $d_{3/2}$ doublets with a branching ratio 3:2 and separation of 3.15 eV. The spectrum of the $c(2 \times 2)$ MoO_3 monolayer (1) was fitted with two components with Mo $d_{5/2}$ binding energies (BE) of 230.9 eV (A, green line) and 232.3 eV (B, red line), related to the 5-fold coordinated Mo atoms inside the domains and at their boundaries, respectively, as established previously [3]. The B-component has a spectral weight of about 40%, perfectly in line with the percentage of the Mo atoms located at the domain boundaries. Their higher binding energy with respect to the Mo atoms within the domains is due to the extra charge transferred from the Pd substrate to the O atoms at the boundaries, required to compensate the edge polarity in the MoO_3 monolayer [17]. In spectrum 3, a third component doublet with Mo $d_{5/2}$ BE of 229.6 eV (C, blue line) was added to account for the increased spectral weight at the lower BE side. The pristine components A and B become broader, corresponding to the reduced structural order in the $c(2 \times 2)$ phase observed in STM. In spectra 5 and 7, where a (4×4) pattern is developed in the LEED, the component C grows at the expense of the A and B components, and its BE shifts slightly downwards to 229.4 eV. The decay of the

pristine surface components is fully in line with the progressive loss of terminal O species detected in STM, whereas the increase of the C component is the result of the increasing area of the oxide layer left behind (Fig. 3). This indicates that the core-level component C may be associated with Mo atoms with a lower O coordination, possibly fourfold planar in the reduced layer. Eventually, spectrum 10, corresponding to the (3x3) phase, contains only two core level components, a major one with Mo $d_{5/2}$ BE of 229.3 eV (C) and a minor one at 228.5 eV (D, orange line), implying an additional reduction of the Mo-O coordination number from 4- to 3-fold in the (3x3) Mo-oxide structure.

The binding energies of the Mo $3d_{5/2}$ core level components A, B, C, and D, encountered during the reduction of the $c(2 \times 2)$ - MoO_3 layer on Pd(100), cannot be directly compared to BE values reported for different possible oxidation states in bulk oxides, such as Mo^{6+} (232.6 eV), Mo^{5+} (231.2 eV), and Mo^{4+} (229.8 eV) [35-37]. On the one hand, the strong oxide-metal interfacial bonding and the charge screening of the metal substrate may significantly modify both the initial and final states in the photoemission process [38]. Moreover, the reduced Mo-O coordination number in the 2D oxide layer may result in binding energies completely different than in their bulk counterparts. Nevertheless, the evolution of the Mo 3d components to lower binding energies testifies the progressive reduction of the $c(2 \times 2)$ - MoO_3 layer upon thermal annealing.

4. Computational results

In this section, we present the calculated structural and electronic characteristics of the oxide phases observed in the experiments upon progressive reduction of the MoO_3 monolayer. Computational models focus on either the observed boundary configurations of larger MoO_3 domains obtained at early reduction stages (reconstructed (10)- and (11)-oriented boundaries) or directly tackle the experimentally resolved reduced oxide phases ($(\sqrt{5} \times \sqrt{5})$, (4x4), and (3x3)) for which the most favored atomic configurations are mainly obtained with the help of the GA-driven global optimization approach. Since the observed sequence of formation of intermediate phases may be influenced by the reduction kinetics, in the following we will present them following their decreasing stoichiometry. In each case a special attention is given to the energetics of oxygen addition and extraction.

4.1. Initial O-rich phases

The initial molybdenum oxide monolayer on Pd(100) consists of square-shaped domains with well structured, stoichiometric $c(2 \times 2)$ - MoO_3 interior, separated by narrow (10)-oriented domain boundaries (Fig. 1b). It has been shown [16,17] that, under the initial experimental conditions, all cations at the domain boundaries preserve their 5-fold environment (Fig. 1e), which produces a considerable overall oxygen excess with respect to the MoO_3 stoichiometry. Typically, for the observed domain size of about $3.5 \times 3.5 \text{ nm}^2$, as much as 40% of the Mo atoms are located at their boundaries so that the overall film composition is close to $\text{MoO}_{3.2}$. It has been pointed out that, since cations both in the domain interior and at the boundaries display their maximal 6+ oxidation state, the excess oxygen atoms are stabilized by a substantial electron transfer from the Pd substrate.

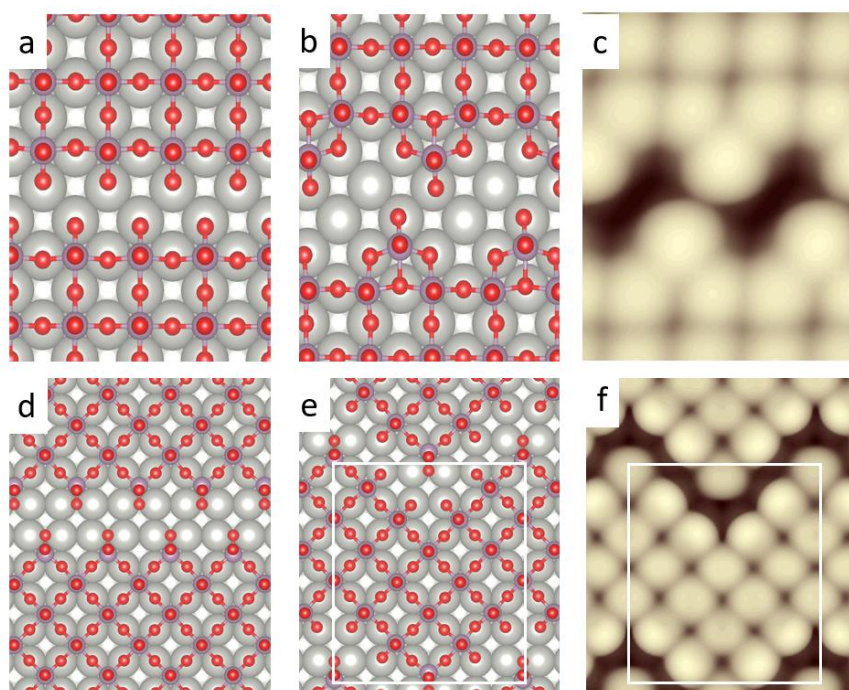


Fig. 7. Atomic structures and simulated STM images of structural details of various initial O-rich configurations: straight (a) and reconstructed (b-c) (10)-oriented boundary; (11)-oriented boundary (d); zig-zag (6x7) phase (e-f). Oxygen, molybdenum and palladium atoms are shown as red, blue, and grey circles, respectively. For a detailed representation of atomic structures see Supplementary Material, Fig. S1.

Removal of a terminal oxygen atom from a Mo cation located in the domain interior (labelled M_{51} in the following, to highlight its 5-fold coordination, and the presence of a single $\text{Mo}=\text{O}$ bond) costs an average energy of $E_{\text{vac}} = 2.42 \text{ eV}$, larger than that at the (10) boundaries (five-fold coordinated Mo bonded to two terminal oxygens and labelled M_{52}), where average $E_{\text{vac}} = 2.17 \text{ eV}$. As a consequence, an initial reduction step will to a large extent preserve the $c(2 \times 2)$ -

structure of the domain interiors, but rather impact their boundaries. Indeed, the present experiments reveal three mechanisms of boundary modification. First, the net decrease of the boundary length associated to the enlarged domains (about $6.5 \times 6.5 \text{ nm}^2$, Fig. 2) induces a reduction of the overall oxygen content to about $\text{MoO}_{3.1}$. Second, due to its substantial energy expense, the removal of terminal oxygens destabilizes the straight (10) boundaries in favour of reconstructed ones. A triangular reconstruction, Fig. 7b-c, observed experimentally (Fig. 2), reduces the number of $\text{Mo}=\text{O}$ groups as to produce a stoichiometric boundary, while preserving the cation 5-fold coordination (instead of 4-fold at the reduced (10) edges, M_{41}). Third, (11)-oriented boundaries, Fig. 7d, start forming at the domain periphery, in coexistence with the reconstructed (10) ones, making the observed domains shape less regular, Fig. 2. The better stability of 4-coordinated cations at the (11) boundaries is due to the fact that two of their four oxygen neighbours are terminal (M_{42}), thus enabling a more thorough relaxation into a local tetrahedral environment. This contrasts with the M_{41} cations issued from oxygen removal from the (10) edges. As a consequence, the stoichiometric (11)-oriented boundaries display a formation energy (0.13 eV/A) close to that of the triangularly reconstructed (10) ones (0.12 eV/A).

Interestingly, 4-fold coordinated cations with two terminal oxygens (M_{42}), are also present in the zig-zag (6×7) phase, Fig. 7e-f, which is observed inside the enlarged domains upon the initial annealing steps, Fig. 2. Under the reducing conditions, the corner M_{42} cations of the zig-zagging (10) boundaries do not attach the fifth oxygen atom ($E_{\text{ads}} = 1.15 \text{ eV/O}$), whereas the remaining edge oxygen atoms are as strongly bound as those at the non-reconstructed (10) boundaries ($E_{\text{vac}} = 2.1\text{-}2.3 \text{ eV/O}$). Despite O-rich $\text{MoO}_{3.22}$ stoichiometry of the (6×7) phase, the boundary-related effects described above make the overall film oxygen content gradually diminish during the reduction process.

In summary, our findings demonstrate that during the initial reduction stage of O-rich MoO_3/Pd ML, the oxygen excess is gradually eliminated by changes in the length, orientation, and atomic structure (reconstructions) of the domain boundaries. It is noteworthy that the oxygen loss is most readily accommodated by specific 4-fold coordinated cations, which have two terminal oxygen atoms.

4.2. Reduced phases

Beyond the initial reduction, the $c(2 \times 2)$ structure of the domain interiors becomes also modified and much more O-poor, with less or no Mo=O groups. Structural models of the three experimentally observed phases: $(\sqrt{5} \times \sqrt{5})$, (4×4) , and (3×3) , issued from the global optimization are shown in Fig. 8 together with their simulated STM images, and their electronic characteristics are summarized in Tab. 1.

Among the various compositions of the $(\sqrt{5} \times \sqrt{5})$ unit cell explicitly addressed by the structural optimization ($\text{Mo}_2\text{O}_4 - \text{Mo}_4\text{O}_7$), only the Mo_2O_4 configuration, Fig. 8a-b, displays both a good stability and an excellent matching of its simulated STM signature with the experiment. The structure is composed of 3-fold coordinated cations filling the surface hollow sites, interconnected by oxygen atoms into a set of parallel zig-zag 1D chains. Each cation binds to one terminal oxygen (and thus is labelled M_{31}) which, similarly to those at the edges of the pristine domains, is additionally stabilized by a relatively short (2.1 Å) O-Pd bond. Removing this oxygen atom requires a quite substantial amount of energy ($E_{\text{vac}} = 2.60$ eV/O) whereas the energy gain upon the attachment of an additional oxygen atom is relatively small ($E_{\text{ads}} = 1.46$ eV/O) and obviously unfavorable under the reducing conditions. This specificity of the oxygen energetics rationalizes the existence of such particularly low-coordinated M_{31} cations in the moderately-reduced MoO_2 phase.

The most favored phase among the considered (4×4) cell compositions ($\text{Mo}_7\text{O}_{14} - \text{Mo}_{10}\text{O}_{20}$) displays a slightly lower stoichiometry of Mo_9O_{17} ($\text{MoO}_{1.9}$) and is principally composed of 3- and 4-fold coordinated cations (M_{30} and M_{40}) interconnected by oxygen atoms into 4- and 5-membered cationic rings, Fig. 8c-d. The film structure may be seen as made of building blocks (indicated with dashed line in Fig. 8c), consisting of a central 4-fold coordinated cation surrounded by four equivalent 3-fold coordinated ones. Contrary to the initial O-rich phases, most of the interconnecting oxygens relax outward and virtually no interfacial O-Pd bonds are formed. A single Mo=O group per unit cell is preserved (M_{51}), and relaxes strongly outward in order to recover a pyramidal-like local environment similar to that of M_{51} cations in the $c(2 \times 2)$ structure. This relaxation considerably enhances the geometric contribution to the STM contrast produced by the terminal oxygen. Interestingly, this (4×4) phase preserves its underlying structure for both oxygen addition/extraction and formation of a Mo vacancy. Regarding the oxygen energetics, desorption of the terminal one ($E_{\text{vac}} = 2.30$ eV/O) requires considerably more O-lean conditions, but the quite large gain of energy upon O adsorption at one of the available

M_{40} cations ($E_{\text{ads}} = 1.87$ eV/O) suggests the possibility of small oxygen uptake under the experimental conditions.

Finally, simulations show that the very stable (3x3) phase observed at the end of the reduction process displays the most O-poor stoichiometry Mo_5O_8 ($\text{MoO}_{1.6}$). It involves only two types of cations per unit cell, a single 4-fold coordinated one (M_{40}) and four 3-fold coordinated ones (M_{30}), Fig. 8e-f, forming the same building blocks as in the (4x4) phase. The decrease of oxygen content compared to this latter thus proceeds by an increase of the M_{30}/M_{40} ratio due to larger ring sizes. Consistently with its O-lean character, the film does not expose any terminal oxygen atoms, so that the formation of any oxygen vacancy would involve breaking of two Mo-O bonds and thus costs much energy. Interestingly, the most stable oxygen adsorption site is not at the M_{40} cation which, because of the in-plane strain, could not relax into a local pyramidal-like environment. Instead, ad-oxygen binds to the hollow site between the four M_{30} cations, with a moderate adsorption energy of $E_{\text{ads}} = 1.74$ eV/O, which suggests that such more O-rich, Mo_5O_9 configuration ($\text{MoO}_{1.8}$) may not be stable under the most reducing conditions.

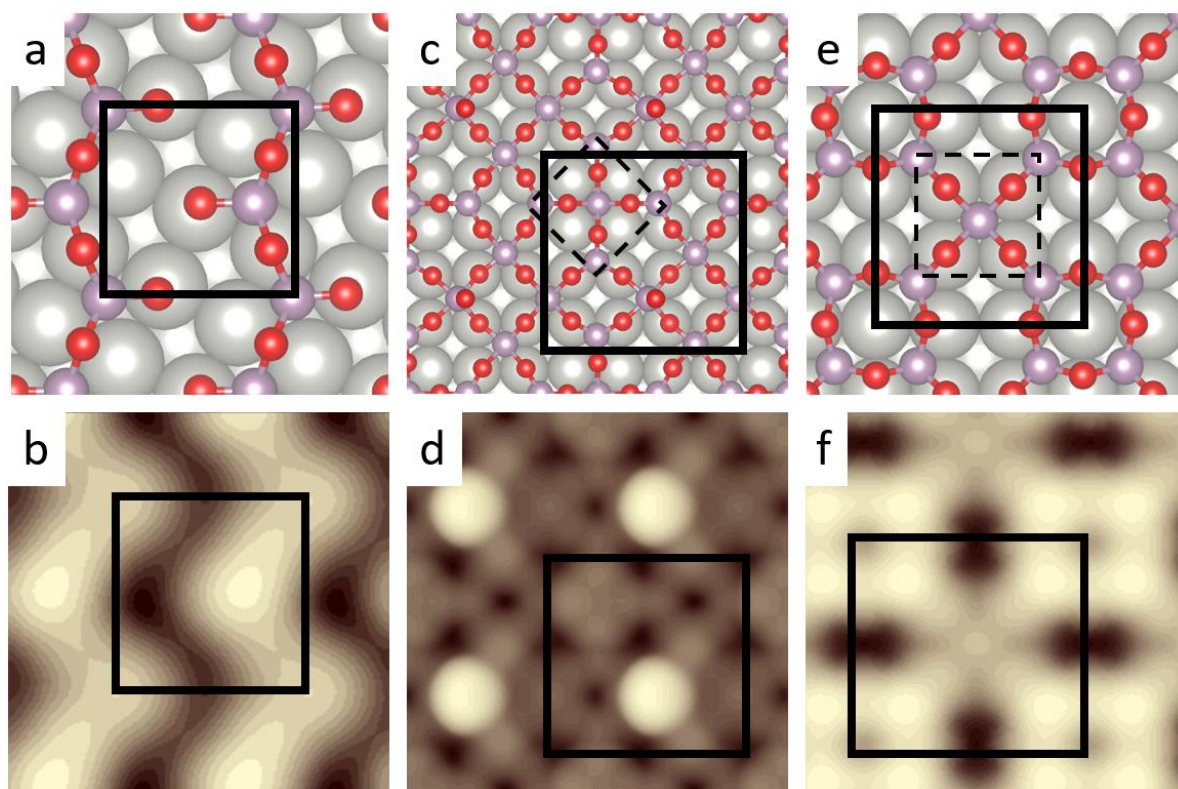


Fig. 8. Atomic structures and simulated STM images of the reduced MoO_x phases: $(\sqrt{5} \times \sqrt{5})$ (a-b), (4x4) (c-d), and (3x3) (e-f). The corresponding surface unit cells are indicated. Oxygen, molybdenum and palladium atoms are shown as red, blue, and grey coloured circles, respectively. For a detailed representation of atomic structures see Supplementary Material, Fig. S2.

Concomitantly with their different stoichiometries and atomic structures, also the electronic characteristics of the three reduced phases differ substantially from those of both the initial O-rich films and the stoichiometric $c(2 \times 2)$ - MoO_3 structure of the domain interiors. The first and most revealing feature is the large variation of the charge borne by the Pd substrate (q_{Pd}), which changes from positive to negative as the reduction proceeds. Indeed, in the O-rich and stoichiometric cases [(6x7) and $c(2 \times 2)$ configurations in Tab. 1], positive values of q_{Pd} show that the substrate transfers its electrons to the oxide film, both along the interfacial iono-covalent O-Pd bonds [stoichiometric $c(2 \times 2)$ phase] and in order to stabilize the possible oxygen excess [O-rich (6x7) phase and initial (10) boundaries]. In stark contrast, the three reduced oxide films transfer a substantial part of their electrons towards the Pd substrate (strongly negative values of q_{Pd}), thus stabilizing cation oxidation states larger than those suggested by the film stoichiometry. Such an effect has already been identified in a variety of metal-supported oxide films [39-43], and has been linked to the existence of a band offset between the oxide films and the electronegative metal substrate [44]. The resulting cation oxidation states could be estimated from their combined electronic signatures (Bader charges, magnetic moments and LDOS). With this in mind, the values of q_{Mo} and μ_{Mo} reported in Tab. 1 provide an insight into the cation oxidation states in the three phases. In the (3x3) one, the central M_{40} cation ($q_{\text{Mo}} = 1.8 \text{ e}$, $\mu_{\text{Mo}} = 1.8 \mu_{\text{B}}$) may be assigned a reduced formal 4+ state, while the four surrounding M_{30} ones ($q_{\text{Mo}} = 2.0 \text{ e}$, $\mu_{\text{Mo}} = 0.1 \mu_{\text{B}}$) are likely Mo^{6+} . The (4x4) phase is composed of two similar M_{40}^{4+} cations in the center of the building blocks ($q_{\text{Mo}} = 1.8 \text{ e}$, $\mu_{\text{Mo}} = 1.7 \mu_{\text{B}}$), four M_{40}/M_{30} ones with 6+ oxidation state ($q_{\text{Mo}} = 2.1 \text{ e}$, $\mu_{\text{Mo}} = 0.2 \mu_{\text{B}}$), and a single 5+ one (M_{51} , $q_{\text{Mo}} = 2.4 \text{ e}$, $\mu_{\text{Mo}} = 0.8 \mu_{\text{B}}$) bound to a terminal oxygen. Finally, the two cations in the $(\sqrt{5} \times \sqrt{5})$ phase likely have an intermediate oxidation state between 5+ and 6+. However, in this last case, a relatively small distortion of the local atomic structure results in a differentiation of the cation states into 6+ and 5+, without any significant change of either the film energy or the interface charge transfer.

The above results show that the estimated cation oxidation states in the three reduced phases do not correspond by far to those deduced from the film compositions (average oxidation state 5.5 in the three phases, while stoichiometry would suggest between 3 and 4) and that their considerable enhancement is systematically enabled by an electron transfer to the Pd substrate. As a consequence, Mo cations in 6+ oxidation state, typical for their 5-fold environments in the $c(2 \times 2)$ domains with O-rich boundaries, are also stabilized in the reduced phases in much less dense environments (4- and even 3-fold coordination), where they coexist with cations in lower oxidation states (M_{40}^{4+} , M_{51}^{5+}). Since both the charge state and the local environment contribute

to the measured binding energies, several Mo signatures are to be expected in XPS experiments and their precise assignment may be intricate and additionally complicated by the coexistence of different phases in the oxide layer. However, in the unique (3x3) phase stabilized under the most reducing conditions, the recorded C and D components of the XPS spectrum, Fig. 6e, may likely be associated to the M_{30}^{6+} and M_{40}^{4+} species, found in the DFT model.

	(6x7)	full 1ML	($\sqrt{5} \times \sqrt{5}$)	(4x4)	(3x3)
composition	MoO _{3.2}	MoO ₃	MoO ₂	MoO _{1.9}	MoO _{1.6}
q_{Mo} (e)	2.5, 2.4	+2.4	2.0	2.1, 2.4, 1.8	2.0, 1.8
μ_{Mo} (μ_B)	0.1, 0.8	0.0	0.4	0.2, 0.8, 1.7	0.1, 1.8
q_{Pd} (e/Mo)	+0.32	+0.18	-0.23	-0.31	-0.46
$\Delta\Phi$ (eV)	+1.5	+1.2	+0.3	+0.5	+0.2
Φ (eV)	+6.8	+6.5	+5.6	+5.8	+5.7

Table 1. Electronic characteristics of the observed Pd-supported MoO_x phases of different composition: charges (q_{Mo}) and magnetic moments (μ_{Mo}) on Mo cations, charge of the Pd substrate per cation (q_{Pd}), work function change ($\Delta\Phi$) with respect to its value calculated for the bare Pd(100) substrate ($\Phi=5.3$ eV). Corresponding results for a full MoO₃ monolayer (with no boundaries) are recalled for reference.

Finally, according to DFT calculations, the reduced phases display systematically much smaller work function values Φ than the O-rich ones, which can be assigned to changes in the two main contributions to the total dipole moment [45,46]. On the one hand, the dipole of the oxide film itself is strongly reduced with respect to the c(2x2)-MoO₃ configuration by the removal of Mo=O bonds pointing outwards. On the other hand, the dipole associated with the interface charge transfer is inverted (opposite signs of q_{Pd}), which also reduces Φ . Thus, in absence of any substantial changes of the interface distance, these two contributions act synergistically towards the observed reduction of the work function. In the most reduced (3x3) phase where the outward Mo=O groups are totally absent, the largest interfacial charge transfer (per cell area) is likely the principal responsible for the most pronounced reduction of Φ . We note that the Φ reduction in the ($\sqrt{5} \times \sqrt{5}$) phase is likely impacted by the chain-like structure of the oxide which leaves parts of the substrate uncovered and makes the Φ value the closest to that of the bare Pd(100) surface. Both the general trend and the precise Φ values are in an excellent agreement with the experiment, Fig. 6d.

In summary, O-lean phases with stoichiometries MoO_2 and lower are formed at the second reduction stage. They mostly consist of three- and four-fold coordinated cations, with either very few or none of their oxygen atoms pointing upwards. Consequently, the reduction of oxygen content in these phases is achieved by an increase in the ratio of 3-fold/4-fold coordinated cations and the corresponding increase in ring sizes. Unlike in the initial O-rich phases, electrons migrate from the oxide films to the Pd substrate, leading to cation oxidation states that are significantly larger than those inferred from the film stoichiometry: Mo^{6+} cations, characteristic of the initial O-rich monolayer, are in fact also present in the most reduced phase as well.

5. Discussion

As to gain a global insight into the characteristics of the Pd-supported MoO_x films upon oxygen reduction, we have constructed a simplified energetic approach, similar to that used before for Au-supported NbO_x clusters [32]. Within this model, the film cohesion energy E_{coh} is decomposed into atomic contributions E_{ij} due to each Mo cation in the unit cell: $E_{\text{coh}} = \sum_{\text{Mo}} E_{ij}$, where $i = 3, 4,$ and 5 corresponds to the number of first oxygen neighbors (coordination number Z) and $j = 0, 1, 2, 3$ is the number of terminal oxygen atoms. In this way, E_{51} represents the energy of cations labelled M_{51} which form five Mo-O bonds, of which one is with a terminal oxygen, E_{52} corresponds to that of M_{52} cations, etc. Values of E_{ij} parameters were adjusted as to reproduce the corresponding DFT formation energies of configurations obtained at subsequent steps of the global optimization procedure. Figure 9a shows that, with eight E_{ij} parameters only, the model can quite convincingly approximate DFT results of quite a large number of film structures of different stoichiometry and connectivity. The fitted values of the E_{ij} parameters, Fig. 9b, show a clear dependence on the cation local environment. Focusing first on the supported case (solid red line, full circles), the E_{ij} parameters become more negative (cation stability is enhanced) as the cation coordination Z increases, which corresponds to a general behavior. Moreover, for a given Z , cations bound to more terminal oxygens are more stable, as found before for the supported NbO_x clusters [32].

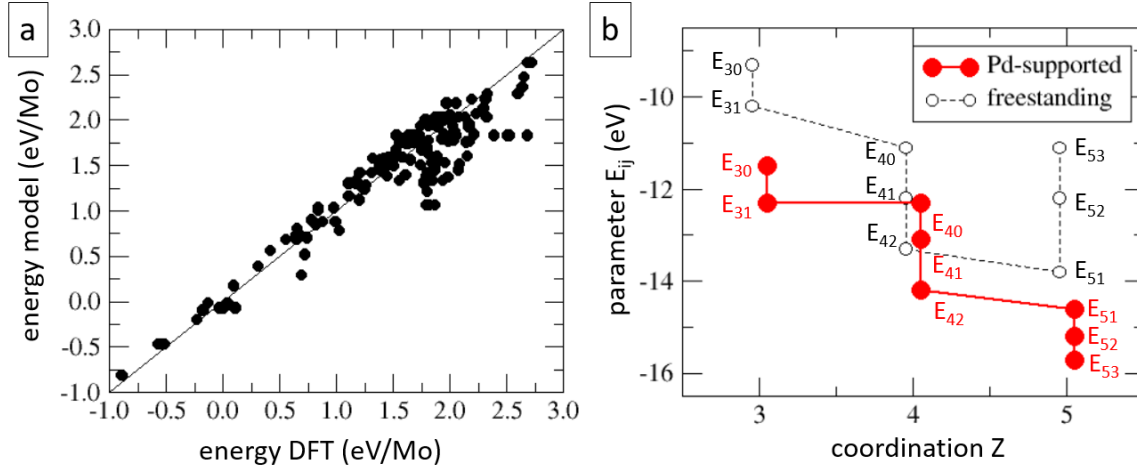


Fig. 9. (a) Parity diagram for the DFT formation energies and the corresponding ones estimated with the atomic parameters E_{ij} . (b) Values of the E_{ij} parameters. Those for the unsupported configurations are included for sake of discussion.

While following very similar trends, the values of supported and unsupported E_{ij} parameters (dashed black line, empty circles) differ in two main respects. First, the interaction with the Pd substrate makes the E_{ij} parameters systematically more negative, thus enhancing the film stability. The effect is stronger for low-coordinated cations (a gain of 2.1 eV for E_{31}) and diminishes progressively with increasing Z (0.9 eV for E_{41} and 0.8 eV for E_{51}). This narrows down the stability differences between cations with different coordination numbers in supported films and makes their coexistence more likely (e.g., $E_{31} \sim E_{40}$). More importantly, the stability behavior of M_{5j} cations as a function of the number j of terminal oxygen atoms is opposite in the supported and unsupported cases. Thanks to the electrons it supplies, the Pd substrate stabilizes the M_{52} and M_{53} cations, while their stability significantly diminishes in the unsupported O-rich objects, showing the difficulty of an insulating MoO_3 phase to accommodate such an oxygen excess.

Aside from explicitly quantifying the impact of the Pd substrate, the E_{ij} parameters also enable an estimation of oxygen stability in the oxide film because energies E_{vac} and E_{ads} and the oxygen conditions corresponding to their formation ($\Delta\mu_{\text{O}} = -E_{\text{vac}}$; $\Delta\mu_{\text{O}} = -E_{\text{ads}}$) can be estimated from E_{ij} differences. In the most relevant case involving breaking/forming a single Mo-O bond, i.e., when the process involves a terminal oxygen atom (thus transforming a M_{ij} cation into a $M_{(i-1)(j-1)}$ or a $M_{(i+1)(j+1)}$ one), $E_{\text{vac}} = E_{(i-1)(j-1)} - E_{ij}$ while $E_{\text{ads}} = E_{ij} - E_{(i+1)(j+1)}$. One can then schematize the reduction pattern in the MoO_3/Pd film as shown in the diagram in Fig. 10.

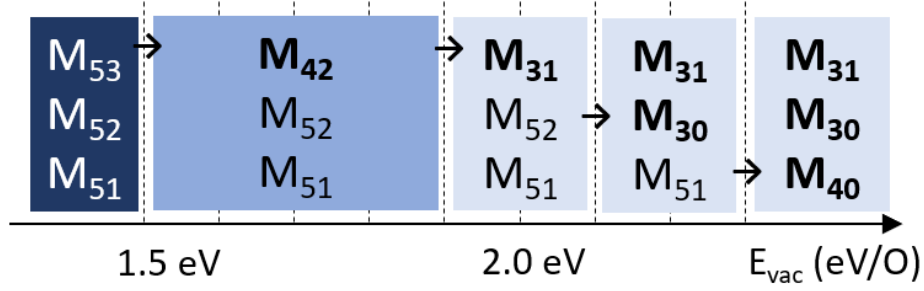


Fig. 10. Schematic representation of the progressive reduction of the different sites of the MoO₃/Pd monolayer domains: domain corners M₅₃, (10) edges M₅₂, and domain interiors M₅₁, represented as a function of oxygen vacancy formation energy E_{vac} (eV/O).

While keeping in mind the approximate character of the E_{ij} values and neglecting any kinetic aspects, it appears that the film reduction proceeds in two principal stages. First, under a relatively wide span of oxygen conditions ($1.5 \text{ eV} \leq E_{\text{vac}} \leq 1.9 \text{ eV}$), the reduction concerns principally the M₅₃ cations and transforms them into M₄₂ ones, such as present at the domain corners, but also, quite abundantly, at the stoichiometric (11)-oriented boundaries and in the zig-zag (6x7) phase which appear at the initial reduction stage. Second, under more O-poor conditions ($E_{\text{vac}} \geq 1.9 \text{ eV}$) also the M₄₂ cations reduce into M₃₁ ones, thus providing the low-coordinated species which constitute the ($\sqrt{5} \times \sqrt{5}$) phase. Subsequently ($E_{\text{vac}} \geq 2.1 \text{ eV}$), M₅₂ cations undergo a reduction into M₄₁, which however are not stable under such O-lean conditions and further reduce into the M₃₀ species. Finally, also the M₅₁ cations reduce into M₄₀ ones. Under the oxygen conditions when the M₅₁ and M₄₀ species still coexist, phases like the (4x4) one (composed of M₃₀, M₄₀, and M₅₁ cations) can form. However, since further reduction definitively eliminates the M₅₁ cations, it leads to the formation of the O-poor (3x3) phase, composed of the M₄₀ and M₃₀ cations.

As to further refine this averaged picture we have analyzed in more detail the M₅₃ \rightarrow M₄₂ reduction, which constitutes one of the main mechanisms of oxygen desorption at the initial reduction stage and provides relatively weakly-bound oxygen atoms of a potential interest for applications. To this goal, we have evaluated the energies of successive O desorption from the O-rich (11)-boundary (composed uniquely of M₅₃ cations) upon its transformation into a stoichiometric one (composed uniquely of M₄₂ cations, Fig. 7d). We find that the oxygen desorption energy visibly increases with the growing coverage of oxygen vacancies: first one-third of O atoms desorbs with a moderate average cost of 1.2 eV/O, while the last one-third requires 1.6 eV/O (leading to an average value $\sim 1.5 \text{ eV/O}$ as shown in Fig. 10). This result reveals a repulsive interaction between vacancies and explains the particularly low oxygen

desorption energy found at the domain corners [16], but also at the corner M_{42} cations in the (6×7) phase, Fig. 7e, where the vacancies are isolated. It also suggests the existence of intermediate ordered phases in which, depending on the local density of the M_{53} sites, the $M_{53} \rightarrow M_{42}$ reduction may take place under different oxygen conditions.

Interestingly, we find a similar increase of the oxygen desorption energy as a function of vacancy coverage upon a progressive $M_{51} \rightarrow M_{40}$ reduction of the $c(2 \times 2)$ phase in the domain interiors. Here, an isolated oxygen vacancy costs 2.2 eV/O, an optimal removal of the first half of oxygen atoms requires 2.3 eV/O, while the second half necessitates a much larger energy of nearly 2.6 eV/O. In this case, however, the O-rich and O-poor parts of the monolayer tend to separate, consistently with the experimental observation of intact $c(2 \times 2)$ patches coexisting with O-poor phases, Fig. 2. Since the local environment of M_{51} and M_{40} cations is different and since the Mo-O bond lengths at the low-coordinated M_{40} cations are contracted, the $c(2 \times 2)$ periodicity is broken and this results in a densification of the reduced film which, as seen in the experiment, Fig. 3, leaves patches of the Pd substrate uncovered.

6. Conclusion

We have performed an exploration of the evolution of the 2D MoO_x nanolayer structures that emerge when the well-ordered MoO_3 monolayer grown on Pd(100) is gradually reduced by temperature. Using atomic resolution STM, LEED, and XPS, the reduction process has been followed step-by-step at the atomic level, and an in-depth picture of the reduction process has been uncovered on the basis of DFT calculations.

During the first thermal annealing stage, the initial monolayer, which consists of $c(2 \times 2)$ domains separated by oxygen-rich boundaries, gets restructured. Oxygen excess is gradually eliminated by changes in the length, orientation, and atomic structure of the domain boundaries: the domain size significantly increases, the boundaries are no longer straight, and triangular reconstruction takes place. Further annealing also induces a restructuring of the domain interiors, and initiates the oxide film fragmentation. Based on calculations, 4-fold coordinated cations with two terminal oxygen atoms appear as the best suited to accommodate this initial oxygen loss. While the oxide film keeps its O-rich composition during this reduction stage, the

Pd substrate positive charge, which stabilizes the oxygen excess, gradually decreases when the overall oxygen content diminishes.

The second reduction stage results in the formation of several O-lean ordered phases with MoO_2 and lower stoichiometry. With either very few or no upward $\text{Mo}=\text{O}$ groups, they are primarily composed of three- and four-fold coordinated cations. Thus, a rise in the ratio of 3-fold/4-fold coordinated cations and an increase in cation ring sizes are required to further reduce the oxygen content in these phases. In contrast to the initial O-rich phases, electrons migrate to the Pd substrate, resulting in cation oxidation states that are significantly larger than those inferred from the film stoichiometry. Indeed, the calculations show that Mo^{6+} cations, which are typical of the initial O-rich monolayer, are still present in the most reduced phase. We argue that the removal of oxygen atoms pointing outwards and the reversal of interface charge transfer are the principal driving forces of the significant reduction of the surface work function observed during the annealing process.

Finally, the experiment demonstrates that the original $c(2 \times 2)$ structure can be restored upon exposure of the most reduced film to oxygen. This reversibility makes the MoO_3/Pd system promising catalyst for oxidation reactions, which usually necessitate cycling between reducing and oxidizing conditions. Such oxide-on-metal inverse model catalyst system allows also to focus on the promotional effect of catalytically active sites at the metal-oxide phase boundary [2,47], which can be studied within the surface science approach.

ORCID iDs

Svetlozar Surnev <https://orcid.org/0000-0002-9756-0674>

Jacek Goniakowski <https://orcid.org/0000-0003-4647-9566>

Claudine Noguera <https://orcid.org/0000-0002-8665-9695>

Falko P Netzer <https://orcid.org/0000-0001-5617-7225>

References

- [1] P. Mars and D. W. van Krevelen, Oxidations carried out by the means of vanadium oxide catalysts, *Chem. Eng. Sci.* 3 (1954) 41.
- [2] A. R. Puigdollers, P. Schlexer, S. Tosoni, and G. Pacchioni, Increasing oxide reducibility: The role of metal/oxide interfaces in the formation of oxygen vacancies, *ACS Catalysis* 7 (2017) 6493.
- [3] S. Surnev and F. P. Netzer, Tungsten and molybdenum oxide nanostructures: two-dimensional layers and nanostructures, *J. Phys.: Condens. Matter.* 34 (2022) 233001.
- [4] F.H. Jones, K. Rawlings, J. S. Foord, P. A. Cox, R. G. Egdell, and B. M. R. Wanklyn, Superstructures and defect structures revealed by atomic-scale STM imaging of $\text{WO}_3(001)$, *Phys. Rev.* 52 (1995) R14392.
- [5] F. H. Jones, K. Rawlings, J. S. Foord, R. G. Egdell, J. B. Pethica, B. M. R. Wanklyn, S. C. Parker, and P. M. Oliver, An STM study of surface structures on $\text{WO}_3(001)$, *Surface Sci.* 359 (1996) 107.
- [6] F. H. Jones, R. A. Dixon, and A. Brown, Observation of reduced (1×1) terraces on $\text{WO}_3(001)$ surfaces using scanning tunnelling microscopy, *Surface Sci.* 369 (1996) 343.
- [7] R. A. Dixon, J. J. Williams, D. Morris, F. H. Jones, R. G. Egdell, and S. W. Downes, Electronic states at oxygen deficient $\text{WO}_3(001)$ surfaces: a study by resonant photoemission, *Surface Sci.* 399 (1998) 199.
- [8] R. E. Tanner and E. I. Altman, Effect of surface treatment on the $\gamma\text{-WO}_3(001)$ surface: A comprehensive study of oxidation and reduction by scanning tunneling microscopy and low-energy electron diffraction, *J. Vac. Sci. Technol.* A19 (2001) 1502.
- [9] M. Li, E. I. Altman, A. Posadas, and C. H. Ahn, Surface phase transitions and related surface defect structures upon reduction of epitaxial $\text{WO}_3(100)$ thin films: A scanning tunneling microscopy study, *J. Vac. Sci. Technol.* A22 (2004) 1682.
- [10] M. Li, A. Posadas, C. H. Ahn, and E. I. Altman, Scanning tunneling microscopy study of terminal oxygen structures on $\text{WO}_3(100)$ thin films, *Surface Sci.* 579 (2005) 175.
- [11] L. E. Firment and A. Ferretti, Stoichiometric and oxygen deficient $\text{MoO}_3(010)$ surfaces, *Surface Sci.* 129 (1983) 155.
- [12] A. Magneli, Structures of the ReO_3 -type with recurrent dislocations of atoms: Homologous series of molybdenum and tungsten oxides, *Acta Crystallogr.* B6 (1953) 495.
- [13] X. Liao, A. R. Jeong, R. G. Wilks, S. Wiesner, M. Rusu, R. Félix, T. Xiao, C. Hartmann, and M. Bär, Tunability of MoO_3 thin-film properties due to annealing in situ monitored by hard x-ray photoemission, *ACS Omega* 4 (2019) 10985.

- [14] K. Inzani, M. Nematollahi, F. Vullum-Bruer, T. Grande, T. W. Reenaas, and S. M. Selbach, Electronic properties of reduced molybdenum oxides, *Phys. Chem. Chem. Phys.* 19 (2017) 9232.
- [15] X. Deng, S. Y. Quek, M. M. Biener, J. Biener, D.H. Kang, R. Schalek, E. Kaxiras, and C.M. Friend, Selective thermal reduction of single-layer MoO₃ nanostructures on Au (111) *Surface Sci.* 602 (2008) 1166.
- [16] M. Mohammadi, F. R. Negreiros, T. Radlinger, P. Edelmayer, F. P. Netzer, and S. Surnev, Interaction of Na with 2D WO₃ and MoO₃ layers on Pd(100): From doping to 2D bronze formation, *J. Phys. Chem. C* 126 (2022) 3289.
- [17] S. Surnev, J. Goniakowski, M. Mohammadi, C. Noguera, and F.P. Netzer, Evolution of structure and polarity in 2D MoO₃ layers on Pd(100): Interplay of interfacial interactions and polarity, *2D Mater.* 11 (2024) 035024.
- [18] G. Kresse and J. Hafner, Ab initio molecular dynamics for liquid metals, *Phys. Rev. B* 47 (1993) 558.
- [19] G. Kresse and J. Furthmüller, Efficient iterative schemes for ab initio total energy calculations using a plane-wave basis set, *Phys. Rev. B* 54 (1996) 11169.
- [20] P. E. Blöchl, Projector augmented-wave method, *Phys. Rev. B* 50 (1994) 17953.
- [21] G. Kresse and D. Joubert, From ultrasoft pseudopotentials to the projector augmented-wave method, *Phys. Rev. B* 59 (1999) 1758.
- [22] J. P. Perdew, A. Adrienn Ruzsinszky, G. Csonka, O. A. Vydrov, G. E. Scuseria, L. A. Constantin, X. Zhou, and K. Burke, Restoring the density-gradient expansion for exchange in solids and surfaces, *Phys. Rev. Lett.* 100 (2008) 136406.
- [23] V. I. Anisimov, F. Aryasetiawan, and A. I. Lichtenstein, First principles calculations of the electronic structure and spectra of strongly correlated systems: the LDA+U method, *J. Phys.: Condens. Matter* 9 (1997) 767.
- [24] S. L. Dudarev, G. A. Botton, S. Savrasov, C. J. Humphreys, and A. P. Sutton, Electron-energy-loss spectra and the structural stability of nickel oxide: An LSDA+U study, *Phys. Rev. B* 57 (1998) 1505.
- [25] R. F. W. Bader, A quantum theory of molecular structure and its applications, *Chem. Rev.* 91 (1991) 893.
- [26] G. Henkelman, A. Arnaldsson, and H. Jonsson, A fast and robust algorithm for Bader decomposition of charge density, *Comput. Mater. Sci.* 36 (2006) 354.
- [27] J. Tersoff and D. R. Hamann, Theory of the scanning tunneling microscope, *Phys. Rev. B* 31 (1985) 805.

- [28] K. Momma and F Izumi, VESTA 3 for three-dimensional visualization of crystal, volumetric and morphology data, *J. Appl. Crystallogr.* 44 (2011) 1272.
- [29] M. Van Den Bossche, C. Noguera, and J. Goniakowski, Understanding the structural diversity of freestanding Al_2O_3 ultrathin films through a DFTB-aided genetic algorithm, *Nanoscale* 12 (2020) 6153.
- [30] M. Van Den Bossche, J. Goniakowski, and C. Noguera, Structural characteristics of Al_2O_3 ultra-thin films supported on the NiAl(100) substrate from DFTB-aided global optimization, *Nanoscale* 13 (2021) 19500.
- [31] G. Missaoui, P. I. Wemhoff, C. Noguera, J. Goniakowski, and N. Nilius, Chromium oxide thin films on Pt(111): An STM and DFT excursion through the phase diagram, Submitted JPCC.
- [32] S. Wang, Y. Zhu, M. Van den Bossche, J. Goniakowski, C. Noguera, and M. R. Castell, Planar Nb_nO_m clusters on the Au(111) surface. *Small Struct.* 4 (2023) 2300141.
- [33] M. Todorova, E. Lundgren, V. Blum, A. Mikkelsen, S. Gray, J. Gustafson, M. Borg, J. Rogal, K. Reuter, J. N. Andersen, and M. Scheffler, The Pd(100)- $(\sqrt{5}\times\sqrt{5})\text{R}27^\circ\text{-O}$ surface oxide revisited, *Surf. Sci.* 541 (2003) 101.
- [34] P. Kostelnik, N. Seriani, G. Kresse, A. Mikkelsen, E. Lundgren, V. Blum, T. Šikola, P. Varga, and M. Schmid, The Pd(100)- $(\sqrt{5}\times\sqrt{5})\text{R}27^\circ\text{-O}$ surface oxide: LEED, DFT and STM study, *Surf. Sci.* 601 (2007) 1574.
- [35] P. A. Spevack and N. S. McIntyre, Thermal reduction of MoO_3 , *J. Phys. Chem.* 96 (1992) 9029.
- [36] J. - G. Choi and L. T. Thompson, XPS study of as-prepared and reduced molybdenum oxides, *Appl. Surf. Sci.* 93 (1996) 143.
- [37] M. T. Greiner, L. Chai, M. G. Helander, W. - M. Tang, and Z. - H. Lu, Metal /metal-oxide interfaces: How metal contacts affect the work function and band structure of MoO_3 , *Adv. Funct. Mater.* 23 (2013) 215.
- [38] F. P. Netzer, Interfacial oxide layers at the metal-oxide phase boundary, *Surf. Rev. Lett.* 9 (2002) 1553.
- [39] C. Wu, M. R. Castell, J. Goniakowski, and C. Noguera, Stoichiometry engineering of ternary oxide ultrathin films: $\text{Ba}_x\text{Ti}_2\text{O}_3$ on Au(111), *Phys. Rev. B* 91 (2015) 155424.
- [40] S. Wang, J. Goniakowski, C. Noguera, and M. R. Castell, Atomic and electronic structure of an epitaxial Nb_2O_3 honeycomb monolayer on Au(111), *Phys. Rev. B* 100 (2019) 125408.
- [41] J. Goniakowski and C. Noguera, Properties of metal-supported oxide honeycomb monolayers: M_2O_3 and $\text{MM}'\text{O}_3$ on Me (111) (M, M' = Ti, V, Cr, Fe; Me = Ag, Au, Pt), *J. Phys. Chem. C* 124 (2020) 8186.

- [42] P. I. Wemhoff, N. Nilius, C. Noguera, and J. Goniakowski, Two-dimensional oxide alloys probed at the atomic level: (V,Fe)₂O₃ honeycomb monolayers on Pt(111), *J. Phys. Chem. C* 126 (2022) 5070.
- [43] P. I. Wemhoff, C. Noguera, J. Goniakowski, and N. Nilius, Structure and stoichiometry self-organization in a mixed vanadium–iron oxide honeycomb film on Ru(0001), *J. Phys. Chem. C* 126 (2022) 19947.
- [44] J. Goniakowski and C. Noguera, Properties of M₂O₃/Au(111) honeycomb monolayers (M = Sc, Ti, V, Cr, Mn, Fe, Co, Ni), *J. Phys. Chem. C* 123 (2019) 9272.
- [45] L. Giordano, G. Pacchioni, J. Goniakowski, N. Nilius, E. Rienks and H.-J. Freund, Interplay between structural, magnetic, and electronic properties in a FeO/Pt(111) ultrathin film, *Phys. Rev. B: Condens. Matter Mater. Phys.* 76 (2007) 075416.
- [46] J. Goniakowski and C. Noguera, Polarization and rumpling in oxide monolayers deposited on metallic substrates, *Phys. Rev. B: Condens. Matter Mater. Phys.* 79 (2009) 155433.
- [47] F. P. Leisenberger, S. Surnev, G. Koller, M. G. Ramsey, and F. P. Netzer, *Surf. Sci.* 444 (2000) 211.